PNAS
RESEARCH ARTICLE | PHYSICS

Topology and kinetic pathways of colloidosome assembly and disassembly

Raymond Adkins[a,b], Joanna Robaszewski[a,c], Seungwoo Shin[a], Fridtjof Brauns[d], Leroy Jia[e], Ayantika Khanra[f], Prerna Sharma[f,g], Robert A. Pelcovits[h], Thomas R. Powers[h,i], and Zvonimir Dogic[a,1]

Affiliations are included on p. 7.

Edited by Noel Clark, University of Colorado Boulder, Boulder, CO; received January 16, 2025; accepted July 16, 2025

Closed capsules, such as lipid vesicles, soap bubbles, and emulsion droplets, are ubiquitous throughout biology, engineered matter, and everyday life. Their creation and disintegration are defined by a singularity that separates a topologically distinct extended liquid film from a boundary-free closed shell. Such topology-changing processes are of fundamental interest. They are also essential for intercellular transport, transcellular communication, and drug delivery. However, studies of vesicle formation are challenging because of the rapid dynamics and small length scale involved. We develop fluid colloidosomes, micrometer-sized analogues of lipid vesicles. The mechanics of colloidosomes and lipid vesicles are described by the same theoretical model. We study colloidosomes close to their disk-to-sphere topological transition. Intrinsic colloidal length and time scales slow down the dynamics to reveal colloidosome conformations in real time during their assembly and disassembly. Remarkably, the lowest-energy pathway by which a closed vesicle transforms into a flat disk involves a topologically distinct cylinder-like intermediate. These results reveal aspects of topological changes that are relevant to all liquid capsules. They also provide a robust platform for the encapsulation, transport, and delivery of nanosized cargoes.

vesicles | topological transformations | shape morphing | kinetic pathways

Controlling the shape and topology of thin elastic sheets is essential for creating reconfigurable and adaptable materials. For inspiration, one can turn toward living matter, where shape morphing enables diverse life-sustaining processes. On macroscopic scales, plants grow sheet-like tissues into intricate leaves and flowers that reconfigure in response to sunlight (1, 2). At the mesoscopic scale, micrometer-thick epithelial sheets undergo highly choreographed morphological and topological transitions to assume complex shapes that define three-dimensional organs (3, 4). At subcellular scales, nanometer-thick lipid bilayers are a distinct category of thin sheets that lack in-plane shear modulus but form complex shapes and topologies (5–9). Translating these structures into the realm of synthetic materials represents a challenge but also a unique opportunity to generate new categories of responsive soft materials. For example, patterning in-plane strains into mesoscale stimuli-responsive solid-elastomeric sheets generated designable and controllable three-dimensional shape morphing materials (10–13). On microscopic scales, lipid vesicles inspired the creation of synthetic analogues with potential applications in transport, encapsulation, and drug delivery (14–19).

We seek to control the morphology and topology of fluid membranes by balancing the bending and edge energy. The edge energy of a flat disk increases with its size, while the bending energy of the edgeless spherical vesicles is size independent (20–23). Thus, with increasing size, the edge energy destabilizes a flat disk, inducing a mechanical instability that generates edgeless vesicles. To study such transitions, we develop fluid colloidosomes, which are colloidal analogs of lipid vesicles, assembled from monodisperse submicrometer-long rod-like particles. By modulating colloidosome size in situ, we balance the edge and bending energy to control transitions between vesicle-like spheres and disks in real-time. In particular, we elucidate the complex vesicle disassembly pathways involving intermediate states, whose topologies are more complex than both the initial and the final state. The rich energy landscape associated with the vesicle-to-disk transition provides a unique platform for controlling the morphology and topology of fluid membranes. Colloidosomes combine desirable features of fluid bilayers, including reconfigurability, self-healing, and topological transitions, with those of solid elastic sheets, such as programmability and control. They may also provide insight into assembly and disassembly pathways relevant to diverse categories of closed vesicle-like materials.

Significance

Lipid membranes are nanometer-thin soap-like films composed of molecules with hydrophilic and hydrophobic segments. To minimize their edge energy, lipid membranes form closed spherical shells or vesicles, ubiquitous and versatile structures in cells with applications in encapsulation, molecular transport, and drug delivery. Controlling vesicle topology is essential in these processes. Rapid dynamics and small scales make it challenging to study the topological transitions of lipid vesicles. We developed fluid colloidosomes, which are micrometer-sized analogs of lipid vesicles assembled from rod-like particles. Their unique features enable real-time visualization of colloidosome assembly and disassembly pathways. Intriguingly, closed vesicles transition to flat disks via an intermediate state that is topologically distinct from the initial and final states.

Author contributions: R.A., J.R., A.K., P.S., R.A.P., T.R.P., and Z.D. designed research; R.A., J.R., S.S., F.B., L.J., and A.K. performed research; R.A., J.R., F.B., L.J., and A.K. analyzed data; and R.A., F.B., and Z.D. wrote the paper.

The authors declare no competing interest.

This article is a PNAS Direct Submission.

[1] To whom correspondence may be addressed. Email: zdogic@ucsb.edu.

This article contains supporting information online at https://www.pnas.org/lookup/suppl/doi:10.1073/pnas.2427024122/-/DCSupplemental.

Colloidosomes Minimize Elastic Energy

In the presence of nonadsorbing polymers, charged rod-shaped particles experience attractive depletion interactions that favor their lateral association (24). Such effective interactions can drive the assembly of one-rod-length-thick fluid monolayer membranes, which assume a flat disk-like shape (25–27). Similarly to lipid bilayers (28, 29), colloidal monolayers are described by the Helfrich free energy:

$$E = \int \left[\frac{\kappa}{2}(2H)^2 + \bar{\kappa}K\right]dA + \gamma \int dL, \qquad [1]$$

where H and K are the mean and Gaussian curvatures, κ and $\bar{\kappa}$ are the associated moduli, γ is the edge tension and dA and dL are the surface and boundary elements. It follows that the energy of a flat disk-shaped membrane is $E_{\mathrm{mem}} = 2\gamma\sqrt{\pi A}$, where A is the disk area, while the edgeless spherical vesicle energy is $E_{\mathrm{vesicle}} = 4\pi(2\kappa + \bar{\kappa})$. The vesicle bending energy is size-independent, while the disk energy increases with its size. Therefore, beyond a critical size:

$$A_1^* = 4\pi(2\kappa + \bar{\kappa})^2/\gamma^2 \qquad [2]$$

flat disks are metastable with respect to closed vesicles. Once $A > A_2^* = 4A_1^*$, the disk-to-vesicle transition barrier disappears, and flat disks are unstable. These considerations explain the stability of closed lipid-bilayer vesicles compared to 2D disk-shaped colloidal membranes (30, 31). Both systems have a comparable edge energy of a few hundred $k_{\mathrm{B}}T/\mu\mathrm{m}$ (32) (*SI Appendix*, Fig. S1), but widely different bending moduli. General arguments predict that membrane bending modulus $\kappa \propto (\mathrm{thickness})^n$, where $n \geq 2.5$ (33, 34). Therefore, micrometer-thick colloidal membranes have a bending rigidity that is orders of magnitude greater compared to nanometer-thick lipid bilayers (35), and a much larger A_1^*.

To create colloidosomes, we reduced the critical area where flat disk become unstable A_1^*. For this, we assembled membranes from 385 nm long virus-like rods (nano385), instead of previously used micron-long rods (25). This decreased κ and thus also A_1^*. Simultaneously, to assemble flat membranes beyond their stability, we improved the purity of critical components used in the assembly process (*Materials and Methods*). Upon mixing nano385 and dextran, small disk-shaped membranes formed throughout the sample. Such membranes coalesced laterally (36), growing in size while sedimenting toward the bottom of the chamber. Once at the bottom, the now-large membranes formed dome-like structures (*SI Appendix*, Fig. S4). Reasoning that the gravity suppressed vesicle closure, we inverted the sample and waited for an additional 18 h. At that point, we observed large unilamellar and multilamellar vesicle-like colloidal membranes or colloidosomes (Movie S1). Smaller colloidosomes were nearly spherical (Fig. 1*D*), while larger ones were shaped as biconcave disks (Fig. 1*E*). Isolated axisymmetric colloidosomes are described by their cross-sectional contours (*SI Appendix*, Fig. S3). In a field of view, we observed hundreds of partially or fully closed structures (Movie S1).

To calculate colloidosome shapes, we modified the conventional Helfrich energy to account for gravity and to enforce the constant area and volume (*SI Appendix*, Eq. **S20**) (37). Although the membranes are slightly compressible, bending is less costly than stretching, so we used a Lagrange multiplier to fix the area. Colloidal membranes are porous to the solvent. Their surface-to-surface virus spacing is ∼10 nm, thus they are impermeable to the depleting polymer (500 kDa dextran, $R_g \approx 20$ nm) (38). Therefore, colloidosomes can support differences in osmotic pressure; they can inflate or deflate.

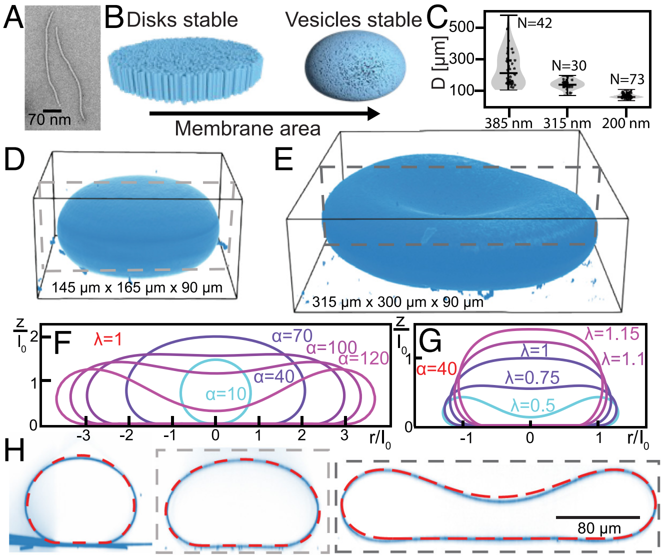

Fig. 1. Colloidosomes minimize membrane elastic energy. (*A*) Electron microscopy image of rod-like nano385. (*B*) Fluid membranes transition from a flat disk to edgeless vesicles with increasing area. (*C*) The maximum diameter of the vesicle, *D*, decreases with decreasing virus length. (*D* and *E*) Smaller colloidosomes have rounded shapes while larger ones sag under gravity. (*F*) Predicted colloidosome shapes with varying α and fixed $\lambda = 1$. (*G*) Colloidosome shapes with varying inflation parameter λ at fixed $\alpha = 40$. (*H*) Cross sections of three colloidosomes using measured values of κ, *V*, and *A*. From *Left* to *Right*: (*Left*) A = 7.87 × 10^3 μm^2, V = 7.0 × 10^4 μm^3; (center) A = 5.49 × 10^4 μm^2, V = 1.1 × 10^6 μm^3; and (*Right*) A = 6.35 × 10^4 μm^2, V = 8.3 × 10^5 μm^3. Dashed lines show the energy-minimizing contour.

The colloidosome shape is controlled by two parameters: a dimensionless surface area $\alpha = A(\sigma g/\kappa)^{2/3}$ and an inflation parameter $\lambda = V/V_0$. Here, σ is the membrane areal mass density, g is gravitational acceleration and A and V are the measured area and volume. V_0 is the volume of the numerically computed energy-minimizing contour computed for the measured surface area, at zero osmotic pressure difference between interior and exterior. For small α, or equivalently small area, curvature energy dominates, generating sphere-like colloidosomes. For large α, the gravitational energy causes sagging deformations (Fig. 1*F*). Similarly, deflated colloidosomes ($\lambda < 1$) assume more biconcave shapes while inflated ones ($\lambda > 1$) are more spherical (Fig. 1*G*).

To test these predictions, we first determined the bending moduli κ and $\bar{\kappa}$. Measurements of thermal fluctuations yielded a mean curvature modulus of $\kappa = 11{,}000 \pm 1{,}000\, k_{\mathrm{B}}T$ (*SI Appendix*, section 1B). Theoretical arguments estimate $\bar{\kappa} = 50\, k_{\mathrm{B}}T$ (*SI Appendix*, section 1D) (39). Since $\bar{\kappa}/\kappa \ll 1$, the Gaussian curvature energy contributes little to the overall shape profile. We then imaged colloidosomes using confocal microscopy, extracted their 2D mesh, and measured their shape, area, and volume (*Materials and Methods*). Theoretical model quantitatively described measured cross-sections without adjustable parameters (Fig. 1*H*). The goodness-of-fit average value was $\langle d^2\rangle/A = 0.015$ with the largest value being $\max(\langle d^2\rangle/A) = 0.05$, where d is the distance between the experimentally measured vesicle contour and the predicted contour (*SI Appendix*, Fig. S5). All colloidosomes were underinflated, with λ decreasing with increasing size. We conclude that colloidosomes minimize the modified Helfrich energy, given a fixed volume and area that are independently extracted from experimental images.

We measured the size distribution of dozens of colloidosomes ($n = 42$) obtaining a mean diameter $D = 250$ µm (Fig. 1*C*), which corresponds to the mean area $A = 64{,}000$ µm^2. The minimum observed diameter was $D = 110$ µm, which corresponds to the surface area $A = 31{,}500$ µm^2. We compare these values to the critical area above which flat disks become metastable (Eq. **2**). To determine A_1^* we quantified the thermal fluctuation of a membrane edge to measure the line tension $\gamma = 700 \pm 40\, k_B T/\mu\mathrm{m}$ (*SI Appendix*, section 1C) (40, 41). When combined with a known value of κ we obtain $A_1^* = 12{,}500$ µm^2, which is less than the smallest experimentally observed vesicle.

Eq. **2** provides a prescription for controlling vesicle size. In particular, decreasing the membrane thickness should strongly reduce the mean curvature modulus κ, generating smaller vesicles. To qualitatively test this prediction, we assembled vesicles composed of 315 and 200 nm long particles. Indeed, we found that the mean and minimum size decreased with decreasing filament length, providing a method to robustly tune the colloidosome size (Fig. 1*C*).

Gravity-Assisted Colloidosome Assembly

The slow dynamics and large length scales revealed a multistep kinetic pathway leading to colloidosome formation. Immediately after inverting the chamber, the pendent colloidosomes underwent gravity-induced elongation, producing hollow tube-like tethers (Fig. 2*A*). These are similar to uniform diameter tethers produced by applying a point force to a lipid vesicle (42–44). However, the diameter of a pendent colloidosome tether increased with height due to the increasing gravitational stresses. The pendent colloidosomes continued extending until either reaching an equilibrium length (*SI Appendix*, Fig. S6) or the chamber bottom. The latter relieved the gravitational stresses and halted extension. A second more rapid phase began with the formation of a crack at the membrane's attachment point with the ceiling, where the gravitational stresses were largest (Fig. 2*B*). Once nucleated, the crack propagated downward, unwrapping the tube-like tether, leaving a twisted ribbon connecting the partially closed colloidosome to the ceiling (Fig. 2*C*) (38). The ribbon kept a single pore open. In the final closure phase, the ribbon thinned and twisted over minutes to hours, eventually rupturing. Subsequently, the pore rapidly closed, completing the topological change to a closed colloidosome (Fig. 2*C* and Movie S2).

To understand the dynamics of pendent colloidosome extension, we numerically solved the modified Helfrich equation with boundary conditions that account for the ceiling attachment (*SI Appendix*, Eqs. **S26–S32**), and varied dimensionless parameters, α and λ (*SI Appendix*, section 3B). Large α, associated with increasing surface area, produced elongated shapes (Fig. 2*D*). Similarly, deflated colloidosomes extended along the z direction ($\lambda < 1$), while inflated ones retracted and became bulbous ($\lambda > 1$) (Fig. 2*E*). We fitted a time series of extending pendent colloidosomes shapes to theoretical predictions. We measured colloidosome area and volume, calculating α and using λ as an adjustable parameter to fit theory to experiments (Fig. 2*F*). Theoretically predicted contours matched experiments, indicating that the extending dynamics was sufficiently slow for a colloidosome to minimize its energy given the particular area and volume (Fig. 2*A*). The area and volume increased throughout the extension (Fig. 2*F*), showing that pendent colloidosomes recruited membrane material from the attachment at the ceiling. Increasing the volume with a constant mass of enveloped dextran would decrease λ. However, measured λ remained close to unity (Fig. 2*G*), suggesting that configurations which perturb the volume incur a significant energetic penalty that resist gravity-driven extension. To maintain the osmotic pressure difference during extension, the dextran must enter the extending colloidosome whose volume is increasing. The membrane is impermeable to the depletant. We conjecture that dextran enters the interior through the opening at the ceiling. Consequently, the extension rate is determined by the rate at which dextran can flow through the top of the pendent colloidosome to equalize the osmotic pressure difference.

Pathways of Colloidosome Disassembly

To control colloidosome morphology and topology in situ, we explored a regime where disks and edgeless vesicles have comparable energetic costs. A buffer exchange device reduced the salt concentration, increasing the electrostatic repulsion between charged rods, causing their evaporation into the background and therefore decreasing the colloidosome area (Fig. 3*A*). Decreasing the area increased the concentration and osmotic pressure of the interior dextran, producing a pressure difference across the membrane, and increasing its tension. Above a critical value, the fluid membrane ruptured, generating a pore which relieved the osmotic pressure difference. The pore remained open until the decreasing membrane area approached the critical area A_1^*. At that point, the pore size increased until the colloidosome transformed into a flat sheet (Fig. 3*B* and Movies S3 and S4).

Slowing the rate of decrease of the vesicle area revealed a distinct multistage disassembly pathway (Fig. 3*G*). Initially, similar to the first pathway, pores nucleated in a slowly shrinking vesicle (Fig. 3*H* and Movie S5). The concentration difference caused the dextran outflow through the pore, reducing the membrane tension and resealing the pore. As the vesicle continuously shrank, this cycle repeated itself. Similar cascades have been observed in lipid vesicles (45–47). The seconds-long transient pores were analogous to the milliseconds-long dynamics observed in lipid vesicles under osmotic shock, mechanical stress, or electroporation (48–53). The second stage was initiated as the vesicle approached the critical area, A_1^*. In this limit, the pores did not reseal. Rather, a second pore, diametrically opposed to the first, nucleated, generating a topologically distinct intermediate structure with two boundaries. With continued area decrease, both pores grew, yielding a cylinder-like intermediate structure, similar to those observed in liposome–talin mixtures (54). Eventually, the cylindrical symmetry of the intermediate hollow cylinder-like was broken as one pore grew in size while the other shrank. The smaller pore resealed, completing the topological transition into a flat disk (Fig. 3*I* and Movie S6).

To gain insight into disassembly pathways, we imaged the intermediate shapes of colloidosomes. Then, using the measured radii of the pore opening as boundary conditions, we calculated the membrane shape that minimized the elastic energy at fixed area. We disregarded gravity in these calculations. The quantitative agreement between the measured and calculated shapes demonstrates that disassembly follows quasi-static (adiabatic) dynamics that can be understood by the energy landscape (*SI Appendix*, Fig. S7). Motivated by this observation, we first calculated the energy associated with a single-opening pathway. For large membranes ($\approx$9,000 µm^2) the global minimum is at zero pore size, indicating the stability of closed colloidosomes (Fig. 3*D*). Decreasing the area to $\approx$7,000 µm^2 creates a local minimum with a nonzero pore size (Fig. 3*E*). At this point, the global minimum is a flat disk, but the vesicle does not unwrap, presumably because

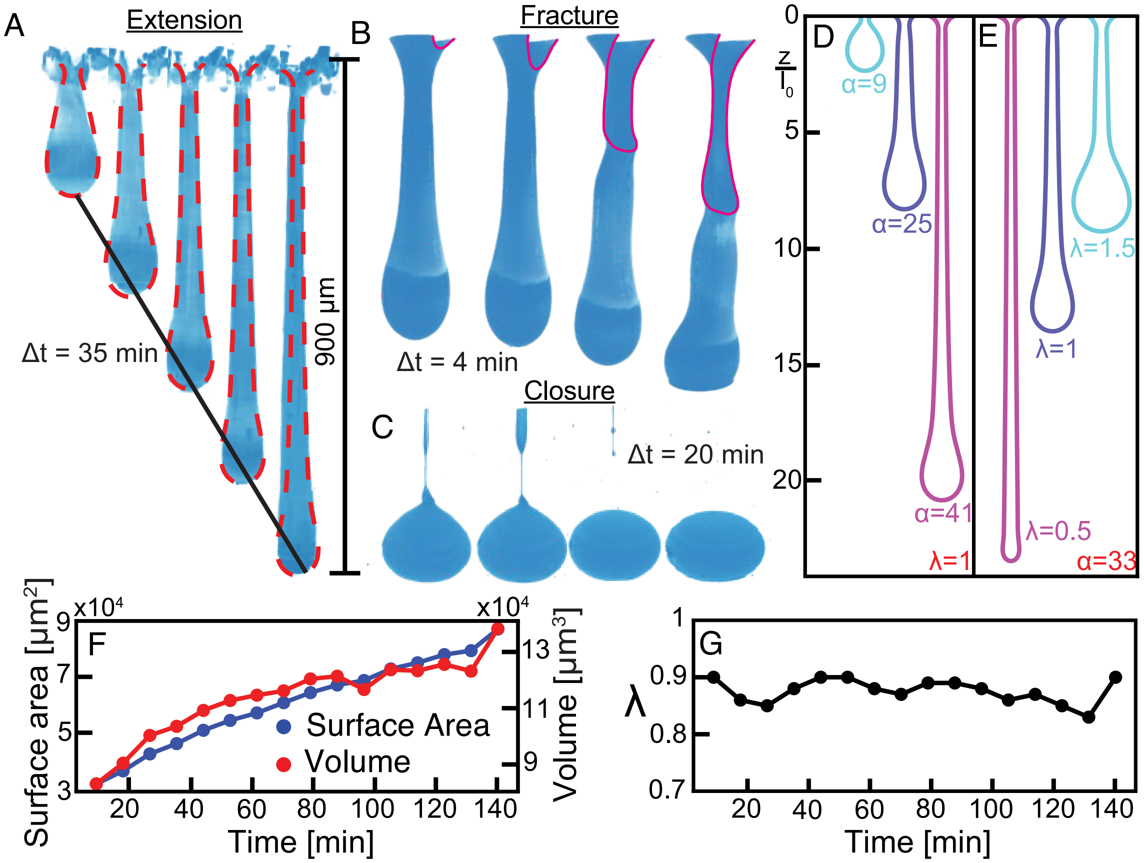

Fig. 2. Gravity-induced extension of pendent colloidosomes. (*A*) A pendent colloidosome extends under gravity. Red lines are theory predictions using measured surface area and λ as a fitting parameter. (*B*) A pendent colloidosome undergoes fracture. (*C*) A twisted ribbon-like tether ruptures, leaving behind a closed colloidosome. (*D* and *E*) Predicted pendent colloidosome shapes with varying α and fixed volume and varying λ and fixed α = 33. (*F* and *G*) Time dependence of surface area, volume, and inflation parameter λ for the extending colloidosome shown in panel (*A*).

thermal fluctuations cannot overcome the energy barrier (55). Decreasing area further ($\leq$5,800 µm^2) eliminates the barrier, at which point the vesicle rapidly unwraps into a flat membrane (Fig. 3*F*). Equally spaced configurations along the energy landscape predicted shapes that agree with the experiment (Fig. 3*C* and Movie S4). Experimentally observed rapid increase in pore size occurs at a critical area, we define at A_0^*, where the energy barrier disappears ($A_0^* \approx$ 5,800 µm^2) (*SI Appendix*, Fig. S8).

To understand the two-pore disassembly pathway, we constructed a 2D energy landscape with varying radii r_1 and r_2 of the two pores for a fixed size (*SI Appendix*, section 3E). Large-area vesicles ($\approx$10,000 µm^2) have a global energy minimum at zero pore size, indicating stable colloidosomes. For intermediate areas ($\approx$7,000 µm^2), the local energy minimum moves away from the origin producing a metastable state with two equal-sized pores (Fig. 3*J*). Notably, one-pore configurations are energetically less favorable than the two-pore state, which explains the preference for two pores given enough time to nucleate them (20). Even though the global minimum for these parameters is a flat disk, vesicle unwrapping is suppressed by an energy barrier. With continuously decreasing area ($\approx$6,200 µm^2) the energy barrier first disappears along the pathway where both r_1 and r_2 increase concurrently (Fig. 3*K*). Once the barrier disappears the steepest gradient descent drives the system toward the saddle point, which corresponds to a tube-like configuration. Subsequently, a spontaneous symmetry breaking expanded one pore while the other one shrank and resealed, thus completing the unwrapping dynamics. Taking equally spaced configurations along a gradient descent of the energy landscape explains experimental observations (Fig. 3*L* and Movie S6). Our work shows that vesicle unwrapping is controlled by two time scales; the rate of area change and the time to nucleate a pore. Importantly, the two-pore configuration has lower energy than the single-pore configuration (*SI Appendix*, Fig. S9). Therefore, slowly shrinking vesicles can overcome the energy barrier associated with second-pore nucleation, which lowers the barrier for disassembly.

Size-Selective Encapsulating Colloidosomes

We investigated the colloidosome's ability to selectively encapsulate and release nano-sized cargoes. We included a low-volume fraction of poly(ethylene glycol) (PEG) labeled with a photoactivatable fluorescent tag into the virus-dextran mixture (*Materials and Methods*). Once vesicles formed, the PEG was photoactivated by UV irradiation, and the fluorescence intensity was visualized. We first used a 1 kDa PEG with a radius-of-gyration $R_g \approx 1$ nm (56). Twenty-three hours after activation, the interior fluorescent intensity of the colloidosome was comparable to the exterior intensity, indicating that the molecules had diffused away through the colloidosome (Fig. 4 *A* and *B*). Next, we used 20 kDa PEG with $R_g = 6.3$ nm. In contrast to the smaller PEG chains, uniform fluorescent signal remained through the colloidosome interior, demonstrating encapsulation (Fig. 4 *C* and *D*). The observed size-selective permeability is consistent with previously measured surface-to-surface spacing between the virus rods of $\sim$10 nm (35). These observations demonstrate that colloidosomes are contiguous size-selective structures that can persistently envelop cargoes and lack defects. While previous

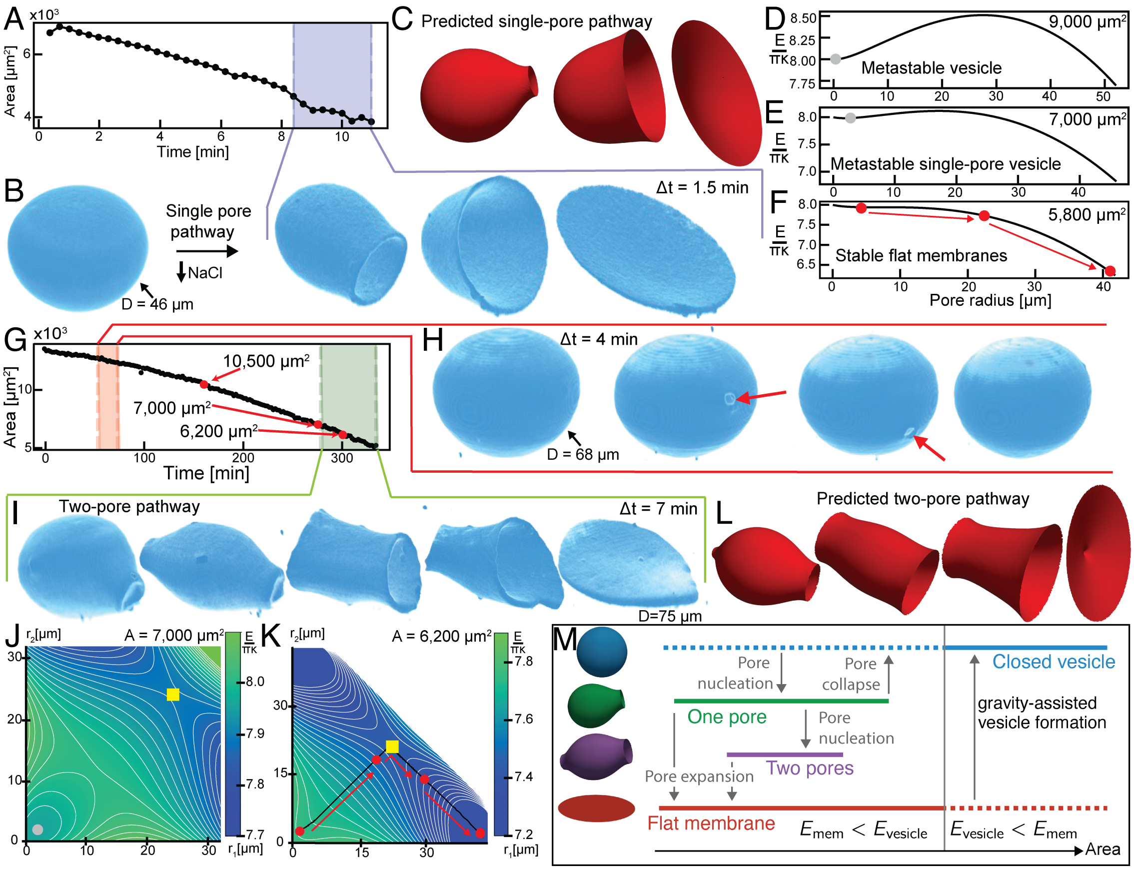

Fig. 3. Vesicle to disk transformation. (*A*) Decreasing vesicle area after buffer exchange. (*B*) Vesicle unwraps by a single pore pathway. (*C*) Predicted vesicle shapes along one pore pathway. (*D*–*F*) Single pore energy landscape with decreasing surface areas. Gray points denote local minima. Conformations associated with the red points are shown in (*C*). (*G*) Colloidosome area undergoing transient pore opening (red) and the two-pore unwrapping (green). (*H*) Transient pore opening. (*I*) Vesicle unwrapping via the two-pore pathway. (*J* and *K*) Two-pore energy landscapes for decreasing surface area, showing the contour plots of the reduced energy $E/(\kappa * \pi)$ as a function of the radii, r_1, r_2, of the pores. Gray points denote local minima; yellow squares denote saddle points. White space in (*K*) denotes a cutoff in the algorithm at large r_1 and r_2, where the energy landscape does not influence the shape dynamics. (*L*) Predicted two-pore pathway, following the gradient of steepest descent on the energy landscape in (*K*). The conformations correspond to the four red points along the energy landscape in (*K*). (*M*) Summary of observed membrane states and the transitions between them as a function of area. The vertical gray line represents the critical area, A_1^*, below which the energetic minima is a flat disk and above which the energetic minima is a closed vesicle. The dotted lines represent metastable states, since vesicles can exist below A_1^* and flat membranes can exist above A_1^*.

studies have made nano-porous materials from sheets of hollow viral rods, our colloidosomes are porous due to the interstitial spacing between viral particles (57). This interparticle spacing is determined by the balance of electrostatic repulsion and depletion attraction, opening the possibility of using colloidosomes as stimuli-responsive size-selective encapsulating agents.

Discussion and Conclusions

We studied pathways that transform a disk-shaped colloidal membrane into a closed colloidal vesicle or colloidosome, as well as the transition back to a flat disk. By balancing edge and bending energy, we prepared marginally stable colloidosomes close to the topological transition associated with their creation and destruction. Experiments and theory revealed the pathway for vesicle disassembly with the lowest energy barrier. Surprisingly, this pathway involves a transient conformation that is topologically distinct from both the initial and the final states.

Let us briefly compare and contrast colloidosomes to extensively studied liposomes. The continuum deformations of both systems are described by the Helfrich energy. However, the colloidal system can be affected by gravity, which needs to be included in theoretical modeling. While they have comparable edge energy, the colloidal membranes have a much larger mean curvature modulus κ. For colloidal membranes $\kappa \approx 10{,}000\ k_BT$ while for lipid membranes the bending modulus is $\approx 10\ k_BT$ (34, 58, 59). This difference dramatically increases the critical area A_1^*, where a flat disk becomes unstable. For liposomes, $A_1^* \approx 0.1\ \mu m^2$, which is magnitudes smaller than $A_1^* \approx 12{,}000\ \mu m^2$ for colloidosomes. The increase in the critical area and the associated slowdown in the dynamics revealed real-time conformations during the topological transitions associated with the vesicle creation and destruction.

Colloidosome assembly and disassembly take place within a complex energy landscape. Above the critical area $A_1^* \approx 12{,}500\ \mu m^2$, a spherical colloidosome has a lower energy than the disk $E_{\text{vesicle}} < E_{\text{disk}}$. However, flat disks with larger sizes can be observed since a large energetic barrier persists between these two configurations. The range of metastable disk states is bounded on the upper end by $A_2^* = 4A_1^* \approx 44{,}000\ \mu m^2$. At this point, the energy barrier for transforming a flat disk into a sphere disappears in the absence of gravity. Gravity considerably influences these transitions. Disk-shaped colloidal membranes settle on the chamber bottom, where they minimize gravitational energy by lying horizontally. Thereafter, gravity suppresses the closure reaction. For this reason, we were not able to experimentally investigate the disk-to-vesicle transition. The assembly of the colloidosome required sample inversion.

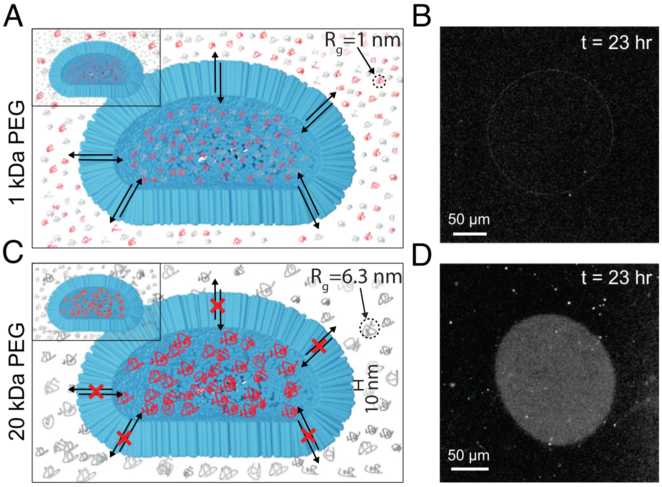

Fig. 4. Encapsulation by colloidosomes. (*A*) Vesicle containing 1 kDa photo activatable PEG. Initially (*Inset*), the photoactivated PEG is inside the vesicle. Over time, the PEG diffuses through the membrane, mixing the active and inactive PEG. (*B*) Lack of contrast between the interior and exterior indicates that the labeled PEG has diffused after 23 h. (*C*) Vesicle containing 20 kDa photoactivatable PEG. Initially (*Inset*), the photoactivated PEG (red) is inside the vesicle. The 20 kDa PEG cannot pass through the membrane, so the photoactivated PEG remains separated from the inactive PEG. (*D*) Fluorescence imaging shows that photoactivated PEG is encapsulated in the vesicle for 23 h.

Changing ionic strength decreases the colloidosome area. This enabled a study of the reverse transition from a closed vesicle to a flat disk. With decreasing area, the vesicle remains metastable even for areas smaller than A_1^*. At some point, below a lower critical lower A_1^*, vesicles with one or two pores have a lower energy than the closed vesicle. In this regime, vesicles with pores are metastable with respect to flat disks. Decreasing the size further eliminates the barrier, and a partially open vesicle transitions into a flat disk. Numerical work indicates that colloidosomes with one pore become unstable once their size is $\approx$5,800 μm^2 (Fig. 3*F*). Experimentally, we observe that the one-pore vesicles transform into flat disks near this surface area (*SI Appendix*, Fig. S8). Colloidosomes with two pores become unstable for areas smaller than $\approx$6,200 μm^2 (Fig. 3*K*). Notably, both of these values are considerably lower than $A_1^* \approx 12{,}500\ \mu\mathrm{m}^2$. For small colloidosomes close to the edge of their stability, the gravitational force is not significant, and the gravity-free model more accurately reproduces experimental observations.

More broadly, we note that previous efforts revealed methods for controlling edge structure and tension of colloidal membranes, as well as their in-plane phase separation, and their Gaussian curvature modulus (39, 60–62). These advances, taken together with a method for creating colloidosomes described here, provide a robust platform for forming structured 2D fluid films and controlling their three-dimensional shapes and topologies. Besides fundamental interest, the principles by which the area and edge tension control the vesicle shape and topology provide a robust platform for encapsulating, transporting, and delivering nanosized cargoes.

Materials and Methods

Phage Production. To produce viral particles, the nano385 phagemid was transfected into cells and then grown in conjunction with a helper phage. The helper phage M13KO7 was grown in *Escherichia coli* strain ER2738 following previously established protocols (63). After viral proliferation, bacteria were removed from the growth media by centrifugation. The helper phage was precipitated out of the media by adding 20 g/L PEG (8 kDa, Sigma-Aldrich) and 20 g/L NaCl, and pelleted by centrifugation (45,000× g for 15 min). The resulting pellet was rinsed and resuspended in virus buffer (2.4 mg/mL Tris-HCl, pH 8.0) at 60 mg/mL to form the helper phage stock solution.

The nano385 plasmid was transformed into a competent F′ *E. coli* strain (NEB C2992H) and grown overnight in 5 mL 2XYT starter cultures containing 100 μg/mL ampicillin (63, 64). Starter flasks containing 50 mL 2XYT were infected with 1 mL of overnight starter culture and helper phage stock solution was added to a final concentration of 2 μg/mL M13KO7 and incubated for 1 h. The 1L growth flasks containing 2XYT, 100 μg/mL ampicillin, 25 μg/mL kanamycin, 200 μg/mL $MgCl_2 \cdot H_2O$ and 120 μg/mL $MgSO_4$ were infected with 5 mL of the starter flask content, and grown with constant shaking at 37 °C. Both nano385 and M13KO7 are extruded from infected bacteria throughout growth. Upon reaching OD 1.5, flasks were removed from incubation and cooled on ice.

To purify the nano385 phagemid, bacteria were removed with one round of low-speed centrifugation (10 min at 4,000× g, Fiberlite F9-6 × 1000 LEX fixed angle rotor, Thermo Scientific) followed by a second high-speed round (15 min, 12,000× g). The supernatant was filtered through a 0.22 μm filter to remove any remaining bacteria. The phage was precipitated by adding 50 g/L PEG 8 kDa and 30 g/L NaCl and pelleted by centrifugation (30 min at 12,000× g) and resuspended in Tris buffer (2.4 mg/mL tris-HCl, pH 8). To increase the phage purity, we performed two additional centrifugation steps (45,000× g for 15 min) to remove bacterial debris, followed by the addition of 50 g/L PEG 8 kDa and 30 g/L NaCl and a second spin to pellet the phage.

After purification, the virus suspension contained a mixture of both M13KO7 and nano385. Adding dextran (MW ≈ 500 k, Sigma-Aldrich) to the mixed growth product induces the isotropic to nematic phase transition in M13KO7 at a lower dextran concentration than the nano385. Dextran was added in steps of 5 mg/mL and centrifuged (22,000× g, 15 min), to condense the nematic phase at the bottom of the centrifuge tube at each step. Gel electrophoresis was used to confirm the separation of M13KO7 and nano385 for each fraction. The fractions that contained only nano385 (typically the 45 mg/mL fraction) were centrifuged (280,000× g, 1 h) to pellet the phage and resuspended in nano385 buffer (7.3 mg/mL NaCl, 2.4 mg/mL Tris-HCl, pH 8.0). Optionally, an additional purification step using anion exchange chromatography could be performed (POROS, GoPure XQ) (65). This procedure dramatically increased membrane size and the frequency of colloidosome formation (Movie S1).

Phage Labeling. To label phages for fluorescent microscopy, we labeled the primary amines of the virus major coat protein with an amine-reactive fluorophore (DyLight-NHS ester 550; Thermo Fisher) according to the dye manufacturer's instructions. Each virus was labeled at a low percent fraction (≈5% of ≈1,150 major coat proteins per phage) to ensure the fluorescent dye does not alter the membrane properties. The labeling percentage was confirmed by a spectrophotometer (Nanodrop One; Thermo Fisher).

Sample Preparation. Samples comprised fluorescently labeled nano385 and 500 kDa dextran in nano385 buffer (7.3 mg/mL NaCl, 2.4 mg/mL tris-HCl, pH 8). Dextran acts as a polymer depletant, inducing an entropic attraction between phages (25). Low-polydispersity dextran (MW 500,000 Da, Sigma-Aldrich) was made using ethanol precipitation which produced significantly cleaner and larger membranes, resulting in more frequent colloidosome formation. To fractionate, ethanol was added dropwise to a solution of 0.2% dextran under vigorous stirring at 23 °C. After reaching 31% (w/w) ethanol, dextran precipitates were removed by centrifugation (20 min at 17,000 g, Fiberlite F9-6 × 1000 LEX fixed angle rotor, Thermo Scientific). Ethanol was then added to a concentration of 32% (w/w) and the precipitate was again collected by centrifugation. The solvent was removed by freeze-dry lyophilization, and the resulting powdered dextran was reconstituted in nano385 buffer to a concentration of 100 mg/mL dextran.

Chambers were made using a microscope slide and coverslip that were coated with acrylamide brush to suppress adsorption and separated by parafilm spacers (66). The number of parafilm layers set the chamber thickness. Four parafilm layers generated ≈500 μm thick chambers which consistently yielded closed colloidosomes. To study the extension dynamics of pendent colloidosome, 3 mm thick chambers were used. Due to membrane sedimentation, 3 mm chambers required a lower final phagemid concentration (0.4 mg/mL) than

500 μm chambers (1 mg/mL) to achieve a similar density of membranes at the surface. All samples were prepared with the final concentration of 54 mg/mL fractionated dextran.

After preparation, the sample was stored overnight with the coverslip facing upward. The next day, curved membranes layered the microscope-glass-side of the chamber (*SI Appendix*, Fig. S4). The sample was then inverted so that the coverslip faced downward. To image membrane extension and tearing, samples were imaged immediately. To image fully formed colloidosomes, the chamber was left inverted for a day or more, and the resulting colloidosomes were imaged.

Production of Vesicles from Shorter Phagemids. To produce vesicles from viral particles shorter than 385 nm, we decreased the length of the phagemid DNA. To produce viral particles that were ≈315 nm in length, we removed the LacZα site from the nano385 plasmid, shortening the length of the phagemid from 2,814 bp to 2,302. This 19% reduction in phagemid length shortened the length of the resulting phage by 19%, resulting in phage of estimated length 315 nm. The phagemid was then transformed into a competent *E. coli* strain, and grown and purified according to an identical protocol as nano385. When making samples, a higher dextran concentration of 65 mg/mL was required to form membranes.

To make phages that were 200 nm in length, we used the pScaf-1512-1 phagemid [Addgene #111402] along with the helper plasmid HP17K07 [Addgene #120346] in the bacterial host XL1Blue (67, 68). These were grown as described previously. Vesicles were formed at 77.1 mg/mL dextran and in a buffer of 7.89 mg/mL NaCl, 2.4 mg/mL Tris-HCl, pH 8.0.

Dialysis Chamber. To perform buffer exchange experiments, we built a custom dialysis device suitable for vesicle formation. Two holes were drilled into a standard microscope glass slide, which was then coated with an acrylamide brush (66). A 20 kDa dialysis membrane was glued on the top surface of the slide, covering the drilled holes. A PDMS buffer exchange chamber was then glued over the top of the dialysis membrane. On the opposing side of the microscope slide, a chamber was formed using a coverslip with 500 μm of parafilm as a spacer. The bottom chamber was filled with the sample (0.4 mg/mL nano385, 54 mg/mL dextran in 7.3 mg/mL NaCl, 20 2.4 mg/mL, pH 8), and sealed with Norland optical adhesive [NOA 61] glue. The top buffer-exchange chamber was filled with nano385 buffer (7.3 mg/mL NaCl, 2.4 mg/mL, pH 8), and sealed with a flexible epoxy. The sample was stored overnight with the coverslip facing up to form membranes on the microscope glass. The chamber was then inverted so that the coverslip faced downward and was stored for an additional day, to form colloidosomes on the bottom coverslip. The flexible epoxy covering the holes in the dialysis chamber was removed, and the chamber was flushed and filled with 2.4 mg/mL Tris-HCl, pH 8 buffer. Salt diffused out of the sample chamber over the course of several hours, while the colloidosome shape change was imaged from below.

Imaging Colloidosomes. To image the fluorescent membranes, we used a spinning disk confocal microscope (Crest X-Light V2) and a Hamamatsu ORCA-Flash4.0 V3 attached to a Nikon Ti2 base. To achieve the speed of imaging required for 3D scans, the camera and the spinning disk were triggered using a Nikon Breakout Box (NI-BB). All images were taken using a water immersion objective to minimize axial distortion. To image sedimented colloidosomes or colloidosome disassembly we used a short-working distance, high NA objective (N40XLWD-NIR, Nikon). To image the several millimeter depth required to study colloidosome extension, we mounted a long-range objective scanner on the scope (V-308 Voice Coil, Physik Instrumente) using a custom bracket, along with a long-working distance water dipping objective (N40X-NIR, Nikon).

Encapsulation Experiments. For encapsulation experiments, we prepared vesicle samples as described previously, with the addition of 5 μg/mL photoactivatable PEG. Photoactivatable PEG was made in lab by conjugating amine-PEG of desired molecular weight with PA Janelia Fluor 646 NHS Ester. Unconjugated dye was removed by overnight dialysis against nano385 buffer, and flash frozen in a stock concentration of 50 μg/mL. Vesicles were formed as before, now with photoactivatable PEG homogeneously distributed throughout the sample. The PA-PEG was activated across a region of interest containing the vesicle using the 365 nm laser line on a Crest X-Light V2 spinning disk microscope, with a 40× objective. The sample was then monitored for fluorescence over the next day. PEG which was sufficiently small diffused through the vesicle and out of the field of view, while large fluorescent PEG molecules remained trapped within the vesicle.

Contouring Colloidosomes. To contour colloidosomes, the 3D confocal images were imported into Fiji (69). Initial rough contours of fluorescent objects in each image were found using the Ridge Detector plugin (70). This generated a mask that roughly contoured the colloidosome but included noise and other membrane objects. To filter these out, we recognize that the z-scans of the colloidosomes are composed of roughly circular cross sections. We then fit each ridge detection image in the z-scan with a circle fit using a RANSAC algorithm in Python. This picked out colloidosome-like objects while rejecting noise and line-like cross-sections that make up other membranes. The Z-stacks of the circular fits acted as an initial point cloud which was converted into a mesh using MeshLab (71). This point cloud was cleaned from outliers using the filters "simplify point cloud" and "Compute Normal for Point Set." These points were then used to construct a surface using the filter "Ball Pivoting." Each mesh was then visually inspected, and self-intersections or holes were manually repaired.

The cleaned meshes were then put through a final round of processing. In the above-described contouring scheme, colloidosomes were assumed to have perfectly circular cross-sections, which introduces unrealistic constraints on the final contour and leads to artifacts. To remedy this, we developed an iterative algorithm to evolve the initial mesh by attracting it toward regions of high intensity. To begin, first-order directional derivatives of the image were taken using a difference-of-Gaussian filter. Each point on the mesh is acted on by a force, $\overrightarrow{F} = \xi \overrightarrow{\nabla} I$, where ξ is a tuned constant and I is the image intensity. This acts to draw each point on the mesh surface toward local regions of high intensity. This algorithm was iterated until convergence. In practice, with the proper choice of ξ, each point moved only several pixels, settling within one hundred iterations. As a final quality control step, each mesh was superimposed on the raw images and manually inspected for alignment. The area and volume of the colloidosomes were then measured from the mesh, using the filter "Compute Geometric Measures."

Data, Materials, and Software Availability. Raw and analyzed data have been deposited in Dryad (DOI: 10.5061/dryad.g4f4qrg03) (72).

ACKNOWLEDGMENTS. This research was primarily supported by the NSF through a grant from NSF-Biomaterials-2308537. A.K. and P.S. acknowledge funding from Department of Science & Technology - Science and Engineering Research Board grants CRG/2019/000855 and WEA/2023/000006. F.B. acknowledges the support of the Gordon and Betty Moore Foundation postdoctoral fellowship (under grant #2919). R.A. acknowledges support by Schmidt Science Fellows, in partnership with the Rhodes Trust. S.S. acknowledges support from the Human Frontier Science Program cross-disciplinary fellowship LT0003/2023-C. R.P. and T.R.P. acknowledge support from NSF Grant CMMI-2020098, and T.R.P. acknowledges support from NSF Materials Research Science and Engineering Centers Grant DMR-2011846. We thank Federico Cao for the valuable discussions. Certain equipment, instruments, software, or materials are identified in this paper in order to specify the experimental procedure adequately. Such identification is not intended to imply recommendation or endorsement of any product or service by National Institute of Standards and Technology, nor is it intended to imply that the materials or equipment identified are necessarily the best available for the purpose.

Author affiliations: [a]Department of Physics, University of California, Santa Barbara, CA 93106; [b]Department of Molecular Biophysics and Biochemistry, Yale University, New Haven, CT 06510; [c]Environmental Laboratory, US Army Engineer Research and Development Center, Concord, MA 01742; [d]Kavli Institute for Theoretical Physics, University of California, Santa Barbara, CA 93106; [e]Applied and Computational Mathematics Division, National Institute of Standards and Technology, Gaithersburg, MD 20899; [f]Department of Physics, Indian Institute of Science, Bangalore 560012, India; [g]Department of Bioengineering, Indian Institute of Science, Bangalore 560012, India; [h]Department of Physics, Brown University, Providence, RI 02906; and [i]School of Engineering, Brown University, Providence, RI 02906

1. U. Nath, B. C. W. Crawford, R. Carpenter, E. Coen, Genetic control of surface curvature. *Science* **299**, 1404–1407 (2003).
2. H. Liang, L. Mahadevan, Growth, geometry, and mechanics of a blooming lily. *Proc. Natl. Acad. Sci. U.S.A.* **108**, 5516–5521 (2011).
3. R. J. Metzger, O. D. Klein, G. R. Martin, M. A. Krasnow, The branching programme of mouse lung development. *Nature* **453**, 745–750 (2008).
4. N. P. Mitchell *et al*., Visceral organ morphogenesis via calcium-patterned muscle constrictions. *eLife* **11**, e77355 (2022).
5. Y. Kozlovsky, M. M. Kozlov, Stalk model of membrane fusion: Solution of energy crisis. *Biophys. J.* **82**, 882–895 (2002).
6. S. D. Conner, S. L. Schmid, Regulated portals of entry into the cell. *Nature* **422**, 37–44 (2003).
7. R. Jahn, T. Lang, T. C. Südhof, Membrane fusion. *Cell* **112**, 519–533 (2003).
8. J. Nixon-Abell *et al*., Increased spatiotemporal resolution reveals highly dynamic dense tubular matrices in the peripheral ER. *Science* **354**, aaf3928 (2016).
9. W. Shin *et al*., Visualization of membrane pore in live cells reveals a dynamic-pore theory governing fusion and endocytosis. *Cell* **173**, 934–945 (2018).
10. Y. Klein, E. Efrati, E. Sharon, Shaping of elastic sheets by prescription of non-Euclidean metrics. *Science* **315**, 1116–1120 (2007).
11. S. Armon, E. Efrati, R. Kupferman, E. Sharon, Geometry and mechanics in the opening of chiral seed pods. *Science* **333**, 1726–1730 (2011).
12. J. Kim, J. A. Hanna, M. Byun, C. D. Santangelo, R. C. Hayward, Designing responsive buckled surfaces by halftone gel lithography. *Science* **335**, 1201–1205 (2012).
13. A. Sydney Gladman, E. A. Matsumoto, R. G. Nuzzo, L. Mahadevan, J. A. Lewis, Biomimetic 4D printing. *Nat. Mater.* **15**, 413–418 (2016).
14. E. Evans, W. Rawicz, Entropy-driven tension and bending elasticity in condensed-fluid membranes. *Phys. Rev. Lett.* **64**, 2094 (1990).
15. U. Seifert, Configurations of fluid membranes and vesicles. *Adv. Phys.* **46**, 13–137 (1997).
16. B. M. Discher *et al*., Polymersomes: Tough vesicles made from diblock copolymers. *Science* **284**, 1143–1146 (1999).
17. A. D. Dinsmore *et al*., Colloidosomes: Selectively permeable capsules composed of colloidal particles. *Science* **298**, 1006–1009 (2002).
18. T. Baumgart, S. T. Hess, W. W. Webb, Imaging coexisting fluid domains in biomembrane models coupling curvature and line tension. *Nature* **425**, 821–824 (2003).
19. Z. Xu, T. Hueckel, W. T. Irvine, S. Sacanna, Transmembrane transport in inorganic colloidal cell-mimics. *Nature* **597**, 220–224 (2021).
20. T. Umeda, Y. Suezaki, K. Takiguchi, H. Hotani, Theoretical analysis of opening-up vesicles with single and two holes. *Phys. Rev. E Stat. Nonlinear Soft Matter Phys.* **1**, 011913 (2005).
21. H. Noguchi, G. Gompper, Dynamics of vesicle self-assembly and dissolution. *J. Chem. Phys.* **125**, 164908 (2006).
22. B. J. Reynwar *et al*., Aggregation and vesiculation of membrane proteins by curvature mediated interactions. *Nature* **447**, 461–464 (2007).
23. M. Hu, J. J. Briguglio, M. Deserno, Determining the Gaussian curvature modulus of lipid membranes in simulations. *Biophys. J.* **102**, 1403–1410 (2012).
24. S. Asakura, F. Oosawa, On interaction between two bodies immersed in a solution of macromolecules. *J. Chem. Phys.* **22**, 1255–1256 (1954).
25. E. Barry, Z. Dogic, Entropy driven self-assembly of nonamphiphilic colloidal membranes. *Proc. Natl. Acad. Sci. U.S.A.* **107**, 10348–10353 (2010).
26. Y. Yang, E. Barry, Z. Dogic, M. F. Hagan, Self-assembly of 2D membranes from mixtures of hard rods and depleting polymers. *Soft Matter* **8**, 707–714 (2012).
27. L. Kang, T. Gibaud, Z. Dogic, T. Lubensky, Entropic forces stabilize diverse emergent structures in colloidal membranes. *Soft Matter* **12**, 386–401 (2016).
28. W. Helfrich, Elastic properties of lipid bilayers: Theory and possible experiments. *Z. Naturforsch. Sect. C J. Biosci.* **28**, 693–703 (1973).
29. H. A. Faizi, C. J. Reeves, V. N. Georgiev, P. M. Vlahovska, R. Dimova, Fluctuation spectroscopy of giant unilamellar vesicles using confocal and phase contrast microscopy. *Soft Matter* **16**, 8996–9001 (2020).
30. W. Helfrich, The size of bilayer vesicles generated by sonication. *Phys. Lett. A* **50**, 115–116 (1974).
31. P. Fromherz, Lipid-vesicle structure: Size control by edge-active agents. *Chem. Phys. Lett.* **94**, 259–266 (1983).
32. T. Portet, R. Dimova, A new method for measuring edge tensions and stability of lipid bilayers: Effect of membrane composition. *Biophys. J.* **99**, 3264–3273 (2010).
33. I. Szleifer, D. Kramer, A. Ben-Shaul, D. Roux, W. M. Gelbart, Curvature elasticity of pure and mixed surfactant films. *Phys. Rev. Lett.* **60**, 1966 (1988).
34. W. Rawicz, K. C. Olbrich, T. McIntosh, D. Needham, E. Evans, Effect of chain length and unsaturation on elasticity of lipid bilayers. *Biophys. J.* **79**, 328–339 (2000).
35. A. J. Balchunas *et al*., Equation of state of colloidal membranes. *Soft Matter* **15**, 6791–6802 (2019).
36. M. J. Zakhary *et al*., Imprintable membranes from incomplete chiral coalescence. *Nat. Commun.* **5**, 3063 (2014).
37. M. Kraus, U. Seifert, R. Lipowsky, Gravity-induced shape transformations of vesicles. *Eur. Lett.* **32**, 431 (1995).
38. A. Balchunas *et al*., Force-induced formation of twisted chiral ribbons. *Phys. Rev. Lett.* **125**, 018002 (2020).
39. A. Khanra *et al*., Controlling the shape and topology of two-component colloidal membranes. *Proc. Natl. Acad. Sci. U.S.A.* **119**, e2204453119 (2022).
40. T. Gibaud *et al*., Reconfigurable self-assembly through chiral control of interfacial tension. *Nature* **481**, 348–351 (2012).
41. L. L. Jia, M. J. Zakhary, Z. Dogic, R. A. Pelcovits, T. R. Powers, Chiral edge fluctuations of colloidal membranes. *Phys. Rev. E* **95**, 060701 (2017).
42. E. Evane, A. Yeung, Hidden dynamics in rapid changes of bilayer shape. *Chem. Phys. Lipids* **73**, 39–56 (1994).
43. T. R. Powers, G. Huber, R. E. Goldstein, Fluid-membrane tethers: Minimal surfaces and elastic boundary layers. *Phys. Rev. E* **65**, 041901 (2002).
44. A. Roux *et al*., A minimal system allowing tubulation with molecular motors pulling on giant liposomes. *Proc. Natl. Acad. Sci. U.S.A.* **99**, 5394–5399 (2002).
45. E. Karatekin *et al*., Cascades of transient pores in giant vesicles: Line tension and transport. *Biophys. J.* **84**, 1734–1749 (2003).
46. K. Oglecka, P. Rangamani, B. Liedberg, R. S. Kraut, A. N. Parikh, Oscillatory phase separation in giant lipid vesicles induced by transmembrane osmotic differentials. *eLife* **3**, e03695 (2014).
47. F. Nomura *et al*., Capabilities of liposomes for topological transformation. *Proc. Natl. Acad. Sci. U.S.A.* **98**, 2340–2345 (2001).
48. O. Sandre, L. Moreaux, F. Brochard-Wyart, Dynamics of transient pores in stretched vesicles. *Proc. Natl. Acad. Sci. U.S.A.* **19**, 10591–10596 (1999).
49. M. Chabanon, J. C. Ho, B. Liedberg, A. N. Parikh, P. Rangamani, Pulsatile lipid vesicles under osmotic stress. *Biophys. J.* **112**, 1682–1691 (2017).
50. J. Moroz, P. Nelson, Dynamically stabilized pores in bilayer membranes. *Biophys. J.* **72**, 2211–2216 (1997).
51. R. Dimova *et al*., Vesicles in electric fields: Some novel aspects of membrane behavior. *Soft Matter* **5**, 3201–3212 (2009).
52. T. Hamada, R. Sugimoto, M. C. Vestergaard, T. Nagasaki, M. Takagi, Membrane disk and sphere: Controllable mesoscopic structures for the capture and release of a targeted object. *J. Am. Chem. Soc.* **132**, 10528–10532 (2010).
53. V. K. Malik, O. S. Pak, J. Feng, Pore dynamics of lipid vesicles under light-induced osmotic stress. *Phys. Rev. Appl.* **17**, 024032 (2022).
54. A. Saitoh, K. Takiguchi, Y. Tanaka, H. Hotani, Opening-up of liposomal membranes by talin. *Proc. Natl. Acad. Sci. U.S.A.* **95**, 1026–1031 (1998).
55. D. H. Boal, M. Rao, Topology changes in fluid membranes. *Phys. Rev. A* **6**, 3037 (1992).
56. K. Devanand, J. C. Selser, Asymptotic behavior and long-range interactions in aqueous solutions of poly(ethylene oxide). *Macromolecules* **24**, 5943–5947 (1991).
57. S. Zhang *et al*., Ultralarge single-layer porous protein nanosheet for precise nanosize separation. *Nano Lett.* **18**, 6563–6569 (2018).
58. R. S. Gracià, N. Bezlyepkina, R. L. Knorr, R. Lipowskya, R. Dimova, Effect of cholesterol on the rigidity of saturated and unsaturated membranes: Fluctuation and electrodeformation analysis of giant vesicles. *Soft Matter* **6**, 1472–1482 (2010).
59. J. Pan, S. Tristram-Nagle, J. F. Nagle, Effect of cholesterol on structural and mechanical properties of membranes depends on lipid chain saturation. *Phys. Rev. E Stat. Nonlinear, Soft Matter Phys.* **2**, 021931 (2009).
60. T. Gibaud *et al*., Reconfigurable self-assembly through chiral control of interfacial tension. *Nature* **481**, 348–351 (2012).
61. P. Sharma, A. Ward, T. Gibaud, M. F. Hagan, Z. Dogic, Hierarchical organization of chiral rafts in colloidal membranes. *Nature* **513**, 77–80 (2014).
62. T. Gibaud *et al*., Achiral symmetry breaking and positive gaussian modulus lead to scalloped colloidal membranes. *Proc. Natl. Acad. Sci. U.S.A.* **114**, E3376–E3384 (2017).
63. E. Wood, Molecular cloning. A laboratory manual. *Biochem. Educ.* **11**, 411 (1983).
64. P. Evans, S. Cook, P. Riggs, C. Noren, Litmus: Multipurpose cloning vectors with a novel system for bidirectional in vitro transcription. *Biotechniques* **19**, 130–135 (1995).
65. R. Monjezi, B. T. Tey, C. C. Sieo, W. S. Tan, Purification of bacteriophage M13 by anion exchange chromatography. *J. Chromatogr. B* **878**, 1855–1859 (2010).
66. A. W. C. Lau, A. Prasad, Z. Dogic, Condensation of isolated semi-flexible filaments driven by depletion interactions. *Europhys. Lett.* **87**, 48006 (2009).
67. F. Praetorius *et al*., Biotechnological mass production of DNA origami. *Nature* **552**, 84–87 (2017).
68. P. M. Nafisi, T. Aksel, S. M. Douglas, Construction of a novel phagemid to produce custom DNA origami scaffolds. *Synth. Biol.* **3**, ysy015 (2018).
69. J. Schindelin *et al*., Fiji: An open-source platform for biological-image analysis. *Nat. Methods* **9**, 676–682 (2012).
70. C. Steger, An unbiased detector of curvilinear structures. *IEEE Trans. Pattern Anal. Mach. Intell.* **20**, 113–125 (1998).
71. P. Cignoni *et al*., "Meshlab: An open-source mesh processing tool" in *Eurographics Italian chapter conference 2008*, V. Scarano, R. De Chiara, U. Erra, Eds. (The Eurographics Association, 2008), pp. 129–136.
72. R. Adkins *et al*., Topology and kinetic pathways of colloidosome assembly and disassembly. Dryad. https://datadryad.org/dataset/10.5061/dryad.g4f4qrg03. Deposited 13 August 2025.